Indian Journal of Chemical Technology
Vol. 28, November 2021, pp. 663-673

Construction of magnetic BiOBr@Fe_3O_4 hybrid nanoparticles via a sol-gel route for photocatalysis application

Yunfeng Song[1], Dongfang Zhang* & Jiaxun Wang
Department of Chemistry, College of Science, Huazhong Agricultural University, Wuhan 430 070, PR China
E-mail: zdfbb@mail.hzau.edu.cn

Received 9 September 2021; accepted 18 October 2021

Development of a highly active visible-light-driven and magnetically recyclable photocatalyst is a challenge for chemical use of solar energy. In this study, Fe_3O_4 nanoparticles (NP), BiOBr and a superior magnetic separable BiOBr@Fe_3O_4 hybrid material have been synthesized via a facile chemical method. The structures, morphological, optical and physical properties of as-synthesized samples have been characterized by X-ray diffraction (XRD), transmission electron microscopy (TEM), ultraviolet-visible (UV-vis) diffuse reflectance spectroscopy, X-ray photoelectron spectroscopy (XPS), Fourier transform-infrared (FT-IR) spectroscopy, photoluminescence (PL) spectroscopy. The photocatalytic activity of the as-synthesized materials is evaluated by photocatalytic degradation of aromatic, heterocyclic organic compound such as methylene blue (MB) and 85% of MB could be removed by BiOBr@Fe_3O_4 hybrid within 60 min. It is found that the composite yield a significantly larger amount of hydroxyl radicals through free radical scavenging test. It is proposed that the observed synergistic effect between Fe_3O_4 and BiOBr is due to the charge transfer between the two oxides, improving the separation of the photogenerated charge carriers via the Z-scheme mechanism, and thus accelerating the photocatalytic degradation of MB and leading to high photocatalytic stability of BiOBr@Fe3O4 material.

Keywords: Fe_3O_4, Magnetic, Photocatalytic, Recycle, Separable

Wastewater discharged from textile and dye industries contain large quantities of organic dyes, which are supposed to be chemically and biologically inert. Some kinds of water soluble and reactive dyes further induce serious damage to the surrounding environment, which can be hardly destroyed with traditional wastewater treatment methods[1-9]. Therefore, the removal of reactive dyes from aqueous solution is necessary and very important[10-36]. Photocatalytic technology is a new type of pollutant degradation technology. Since 1972, two scientists, Fujishima and Honda of the University of Tokyo reported the results of catalytic decomposition of H_2O to produce O_2 and H_2 using TiO_2 as an electrode, the development and research of photocatalytic technology has entered an era of rapid development. Since then, many scientists have conducted in-depth research on photocatalytic technology, and found that photocatalytic reaction has great advantages in water pollution, disinfection and sterilization, energy conservation and emission reduction, etc[37-50]. Water pollutants such as residual pesticides, fertilizers and other pollutants that cannot be decomposed by common catalysts can be decomposed by photocatalysts, and environmentally friendly organic and inorganic substances can be decomposed, which has the advantages of fast reaction rate, high catalytic efficiency, energy conservation, and is therefore widely used in water pollution control, drug degradation, etc[51-71].

During the past decades, photocatalytic degradation of organic dyes by using semiconductor nanoparticles is of growing interest for environmental remediation. Among various photocatalysts, titania has been employed widely in the destruction of organic pollutants due to its low cost, excellent chemical stability, non-toxicity and high activity[72-86]. However, the band gap energy of titanium dioxide photocatalyst is very wide and can only be excited under the irradiation of ultraviolet light, and because the ultraviolet energy of the whole sunlight is very weak, only 2-3%. Therefore, titanium dioxide photocatalyst has this fatal weakness, that is, it cannot make full use of sunlight in photocatalytic reaction. Therefore, it is important and necessary to develop other new visible light catalysts in current era[87-99].

According to the recent survey, various new semiconductors can be used as effective visible light

photocatalysts for substitute TiO_2. BiOBr, as a novel type of semiconductor material, has high catalytic activity for the degradation of toxic organic substances due to its special electronic structure. Due to its simple preparation process and small forbidden band width, BiOBr can react under visible light, so it has a good application prospect to degrade toxic organic pollutants under visible light. BiOBr degradation of pollutants has been widely reported, but its development is limited due to its low photocatalytic efficiency for organic pollutants, and its practical application is relatively few. Research shows that photogenerated carriers of single BiOBr material are easy to recombine, which affects photocatalytic activity[100-102]. However, materials with two-dimensional nano-morphology can be compounded with other materials to construct a new composite catalyst due to their special morphology, which is conducive to effective separation of holes and electrons, and accords with higher catalyst activity. Therefore, the construction of two-dimensional composite catalysts with high activity will become a research hotspot in the future. Morever, these studies seem to not support the fast separation and efficient recycle of BiOBr photocatalysts, i.e., the photocatalysts always remained in a powder state and suspended in aqueous solutions during the photocatalytic reaction, making it difficult to be recovered rapidly in practical.

Magnetic separation water treatment technology is widely used in the field of water treatment as a physical treatment technology, and also shows many advantages. Magnetic separation technology uses the effect of magnetic materials and magazine particles in water to separate, while for non-magnetic materials and weak magnetic materials in water, magnetic inoculation technology can be used to make them become magnetic or more magnetic, and then these materials can be separated by external magnetic field, thus achieving the purpose of separation, purification or recovery. The advantages of magnetic materials including :(1) the sewage treatment speed is fast, the efficiency is high and the capacity is large; (2) the cost is low, and expensive chemical reagents and large-scale complex equipment are not needed; (3) The required site is small and the occupied area is small; (4) the purification device is simple and is beneficial to popularization. To facilitate the fast and efficient photocatalyst recycling, Fe_3O_4 has gained much attention as a result of its advantageous magnetic properties under an external magnetic field. As a kind of ferrite magnetic material with good magnetism, Fe_3O_4 is widely used in magnetic materials and devices which can also be used as a magnetic carrier to obtain a photocatalyst which can be separated and recovered by a magnetic field. Besides, Fe_3O_4 has a wide range of sources, stable structure, low production cost, environmental friendly and other characteristics, so it is applied in photocatalysis aspect. Fe_3O_4 would thus be promising to act as a key building block to construct advanced photocatalysts with superior photocatalytic activity and perfect recycle performances. Therefore, the combination of BiOBr with Fe_3O_4 to form high performance catalyst would be quite meaningful.

At present, the difficult recovery of BiOBr photocatalyst has been affecting its industrial promotion and application. In this paper, BiOBr, Fe_3O_4 and their composite catalysts are synthesized from the problem of water pollution control. The synthesized composite catalyst can not only efficiently decompose methylene blue (MB) dye in water, but also can be conveniently recovered, thus solving the secondary pollution problem of the catalyst. MB (3,7-bis(dimethylamino)-phenothiazine-5-ium chloride) is a widely used organic dye. MB is an aromatic, heterocyclic organic compound, soluble in water, alcohol and chloroform, and belongs to the category of cationic phenothiazine dyes. At room temperature, MB is highly toxic to humans. For these reasons, MB was chosen to be examined as a model pollutant in this work. It was found that the as-made BiOBr@Fe_3O_4 heterostructure system exhibit superior photocatalytic efficiency as compared to bare BiOBr. In addition, the BiOBr@Fe_3O_4hybrid can be easily separated and recycled with the aid of a permanent magnet after each photoreaction process.

Experimental Section

Material preparation

All reagents were analytical grade (AR, China national medicine group chemical reagents Co. Ltd) and used without further purifying. The experimental water is deionized water. In a typical procedure, 0.485 g of bismuth nitrate pentahydrate and 0.357 g of potassium bromide solid, magnetically stirring at room temperature to form a mixed solution, transferring the mixed solution to a high-pressure reaction kettle to maintain a constant temperature of 160°C for hydrothermal reaction for 10 h, cooling to

room temperature when the reaction stops, pouring out the product of the hydrothermal reaction, centrifuging, washing, and drying at 60°C to obtain bismuth bromide solid. According to the above method, sufficient BiOBr samples were prepared and sealed for later use. For the preparation of Fe_3O_4, 0.27 g $FeCl_3$, 0.198 g of glucose, 0.2 g of PEG and 0.1361 g of sodium acetate, magnetically stirring at room temperature to form a mixed solution, transferring the mixed solution to a high-pressure reaction kettle for hydrothermal reaction at a constant temperature of 200°C for 10 hours, cooling to room temperature when the reaction stops, pouring out the product of the hydrothermal reaction, centrifuging, washing and drying at 60°C to obtain ferroferric oxide solid. According to the above method, sufficient Fe_3O_4 samples are prepared and sealed for later use. For the preparation of BiOBr@Fe_3O_4, 0.07 g of ferric tribromide hexahydrate and 1.21 g of bismuth nitrate pentahydrate, dissolving in a solvent, magnetically stirring at room temperature to form a mixed solution, transferring the mixed solution to a high-pressure reaction kettle to maintain a constant temperature of 180°C for hydrothermal reaction for 12 h, cooling to room temperature after the reaction stops, pouring out the product of the hydrothermal reaction, centrifuging, washing, and drying at 60°C to obtain the composite Fe_3O_4@BiOBr.

Characterizations

D8-advan x-ray diffractometer (XRD) was used to test the crystal phase and crystallinity of the samples. The test voltage was 40 kV and the current was 40 mA. Nieolet Magna IR 750 fourier transform infrared spectrometer (FT-IR) was used to carry out infrared test, and potassium bromide was used as substrate background to make tablets. The UV-vis diffuse reflectance absorption spectrum (UV-vis DRS) of the sample was measured by UV-2550 (Shimadzu, Japan) UV-vis spectrophotometer, and the fluorescence spectrum analysis was measured by RF-5301PC fluorescence spectrometer of Shimadzu, Japan. The morphologies and crystal structures of the photocatalysts were verified by transmission electron microscope (TEM, Titan themis 200/Talos 200/ tecnai G2 F30 (FEI)). The optical response ranges of the samples were observed through diffuse reflectance spectra detected by a Varian CARY 500 UV-vis-NIR spectrophotometer equipped with a $BaSO_4$ integrating sphere as reference. The absorption spectra could be converted from the reflection data according to the Kubelka-Munk equation: $F(R)=(1-R)^2/2R$, where R was on behalf of the reflectance. X-ray photoelectron spectroscope (XPS, Escalab 250Xi (Thermo Scientific)) with the Al Kα radiation was performed to investigate the binding energies of Br, O, Bi and Fe.

Photocatalytic activity evaluation

The photocatalytic activities of the as-prepared samples were investigated by the degradation of MB solution at the room temperature. A 300 W Xenon lamp with a cut-off filter (λ>420 nm) was used as the light source. Firstly, 10-3 mol/L aqueous MB solution was diluted into 100 ml, 10-5 mol/L. Then add the as-prepared 50 mg of BiOBr or the equivalent amount of Fe_3O_4@BiOBr sample into a reaction bottle filled with 200 ml of prepared aqueous MB solution, and perform dark adsorption for 60 min to enable the catalyst surface to reach adsorption-desorption equilibrium. Place the reaction bottle in a photoreaction instrument, turn on the magnetic stirrer, and irradiate for 1 h under the above xelon lamp. Every 10 min, 10 ml of supernatant is taken out and centrifuged in a centrifuge for 3 min at a rotation speed of 8000 r/min. Then the absorbance of the separated supernatant is measured. According to Lambert-Beer's Law A = ε BC, the degradation degree of MB aqueous solution is calculated, and the catalytic effect of the prepared photocatalyst is evaluated. According to the above steps, the experiment of photocatalytic degradation of methyl orange aqueous solution with BiOBr and Fe_3O_4@ BiOBr composite catalysts was completed. And complete the spectrogram drawing.

Results and Discussion

Phase and crystallization properties

The phase and crystallization properties of the photocatalyst were determined by XRD analysis. After drying, cooling and grinding the obtained product into powder particles, the composition and phase structure of the powder particles are investugated by X-ray diffractometer, and Bragg formula can be used to express the detection principle of XRD, namely: $2d\sin\theta=n\lambda$, where d represents crystal plane spacing, λ represents the radiation wavelength, n represents the diffraction order, theta is Bragg angle. Several diffraction peak data of the XRD spectrum are compared with the standard diffraction peak data of the measured sample. Figure 1 is an X-ray diffraction spectrum of prepared ferroferric oxide (Fe_3O_4), BiOBr and BiOBr@Fe_3O_4 samples.

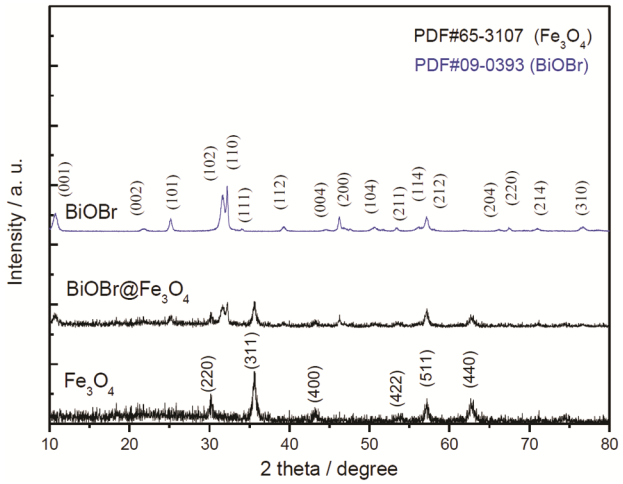

Fig. 1 — XRD patterns of the as-synthesized Fe_3O_4, BiOBr and BiOBr@Fe_3O_4 samples.

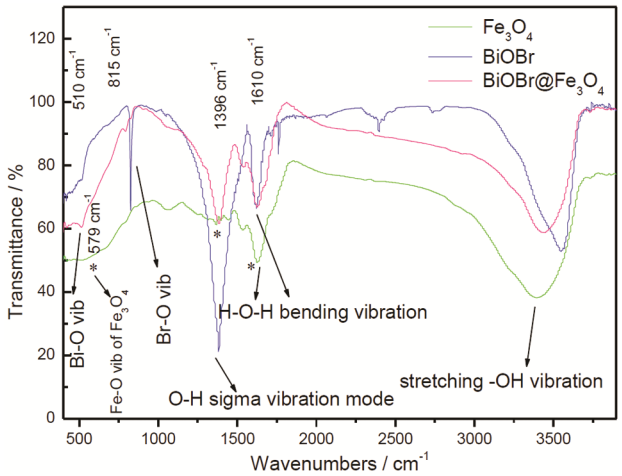

Fig. 2 — FT-IR spectra for as-synthesized Fe_3O_4, BiOBr and BiOBr@Fe_3O_4 samples.

The graph shows XRD patterns of Fe_3O_4, BiOBr and BiOBr@Fe_3O_4 synthesized by a simple chemical co-precipitation method. For Fe_3O_4 nanoparticles, the diffraction peaks appear at 30.5°, 35.4°, 43.0°, 53.4°, 56.9° and 62.5°, which are cubic Fe_3O_4 lattice planes of (220), (311), (400), (422), (511) and (440), respectively. These results are in good agreement with the XRD patterns of Fe_3O_4 nanoparticles reported in JCPDS card (no 65-3107). No characteristic peak belonging to impurity phase (Fe_2O_3 or FeOOH) was observed, indicating that Fe_3O_4 nanoparticles have high purity. The particle size of Fe_3O_4 powder estimated using Scherrer formula is about 30 nm. It is worth noting that all diffraction peaks in the XRD pattern of the BiOBr powder synthesized by an easy co-precipitation method match with the tetragonal BiOBr of the standard XRD pattern (JCPDS card number 09-0393). The diffraction peaks appear at 10.96° 25.16°, 31.69°, 32.22°, 46.21°, 50.67°, 57.12° and 76.69° corresponding to the (001), (101), (102), (110), (200), (104), (212) and (310) planes of high purity BiOBr catalyst. The strong and sharp diffraction peak indicates that the BiOBr catalyst has good crystallinity. Compared with the XRD pattern of the BiOBr material, the composite BiOBr@Fe_3O_4 material has three obvious Fe_3O_4 diffraction peaks at 30.5°, 35.4° and 62.5° respectively, indicating that Fe_3O_4 has been successfully combined with BiOBr.

Figure 2 shows the infrared spectra of Fe_3O_4, BiOBr and BiOBr@Fe_3O_4 samples, the green line corresponds to the IR spectrum of Fe_3O_4 sample, and the observed band of 500-700 cm^{-1} may be related to the telescopic vibration of Fe—O bond. For Fe_3O_4 spectra, the bands at 579 cm^{-1},1396 cm^{-1} and 1610 cm^{-1} (marked with *) show strong absorption bands due to Fe—O bond vibration of iron oxide, and water molecules carried on the reagent surface between 3200-3500 cm^{-1}. The blue line is the IR spectrum line of BiOBr sample. It can be seen from the graph that there are obvious absorption peaks at 815 cm^{-1}, 1396 cm^{-1} and 1610 cm^{-1}, indicating the existence of Br—O, O—H and H—O—H. The pink line is the absorption line after Fe_3O_4 and BiOBr are hybridized. The characteristic absorption band of Fe_3O_4 can still be seen from the IR spectrum of the BiOBr@Fe_3O_4 composite, but the characteristic absorption band of BiOBr is obviously weakened. The result shows that there is no change in substance and structure during the process of Fe_3O_4 and BiOBr coupling, i.e. the obtained composite catalyst contains only Fe_3O_4 and BiOBr components.

Morphology, microstructure and chemical states

Morphology and microstructure of synthesized samples were further investigated by TEM images, as displayed in Fig. 3. As shown in the graph (Fig. 3A), a large number of Fe3O4 nanoparticles (NPs) formed with sphere shapes, and the as-prepared Fe3O4 NPs are irregular spheroid-like with the average diameter of about 30 nm. It is clear from Fig. 3(B) that pure BiOBr exhibits typical two-dimensional lamellar structure, and a large number of irregular layered objects and the nanosheet shape structure of BiOBr can be observed. The length of the plates with lamellar structure is between 100 nm and 120 nm. In Fig. 3(C), the TEM image of BiOBr@Fe_3O_4 shows that the surfaces of Fe3O4 NPs are wrapped with thin l ayers of BiOBr, leading to the formation of

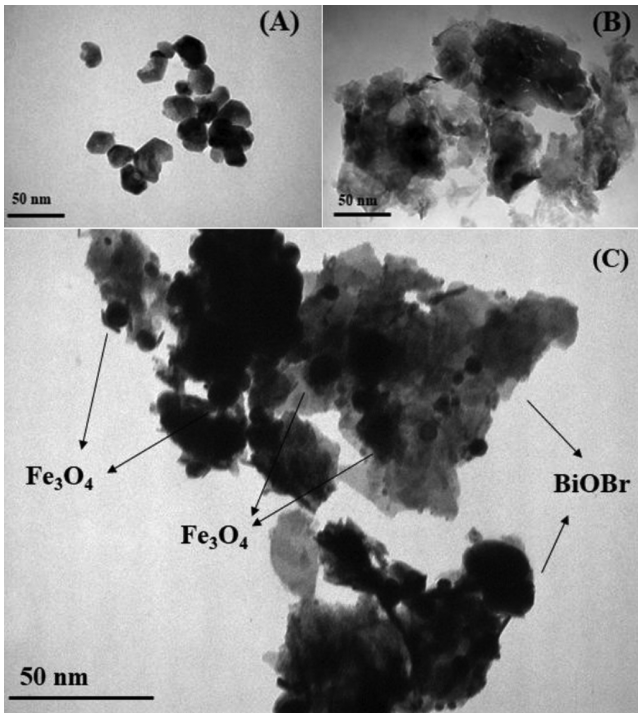

Fig. 3 — The representative TEM images of as-prepared (a) Fe_3O_4 NPs (b) BiOBr plates and (c) BiOBr@Fe_3O_4 samples.

BiOBr@Fe_3O_4 heterostructure. It can be clearly seen that Fe_3O_4NPs are tightly attached to the layered BiOBr, anchored at the edge or surface of BiOBr nanosheet, and indicates that heterojunction has been generated, which is helpful for the transfer of photo-generated electrons and for improving photocatalytic performance. It is evident that the morphology of the as-synthesized BiOBr@Fe_3O_4 is also composed of large lamellar structure with numerous random dispersed Fe_3O_4 NPs decorating on the BiOBr nanosheets, and lots of the pleats proved that the lamellas were ultrathin. The BiOBr is directly coupled with the Fe_3O_4 NPs. Such a structural feature is beneficial for efficient charge carrier separation, which will be discussed later.

The chemical states and surface elemental compositions of materials are investigated by XPS test. The peak positions in all XPS spectra depicted in Fig. 4 have been calibrated with C 1s at 284.8 eV. The typical survey XPS spectra of BiOBr@Fe_3O_4 showed the existence of Fe, Br, Bi and O elements. As displayed in Fig. 4A, the peaks located at 724.7 eV and 711.2 eV are ascribed to Fe 2p1/2 and Fe 2p3/2, respectively. Moreover, no

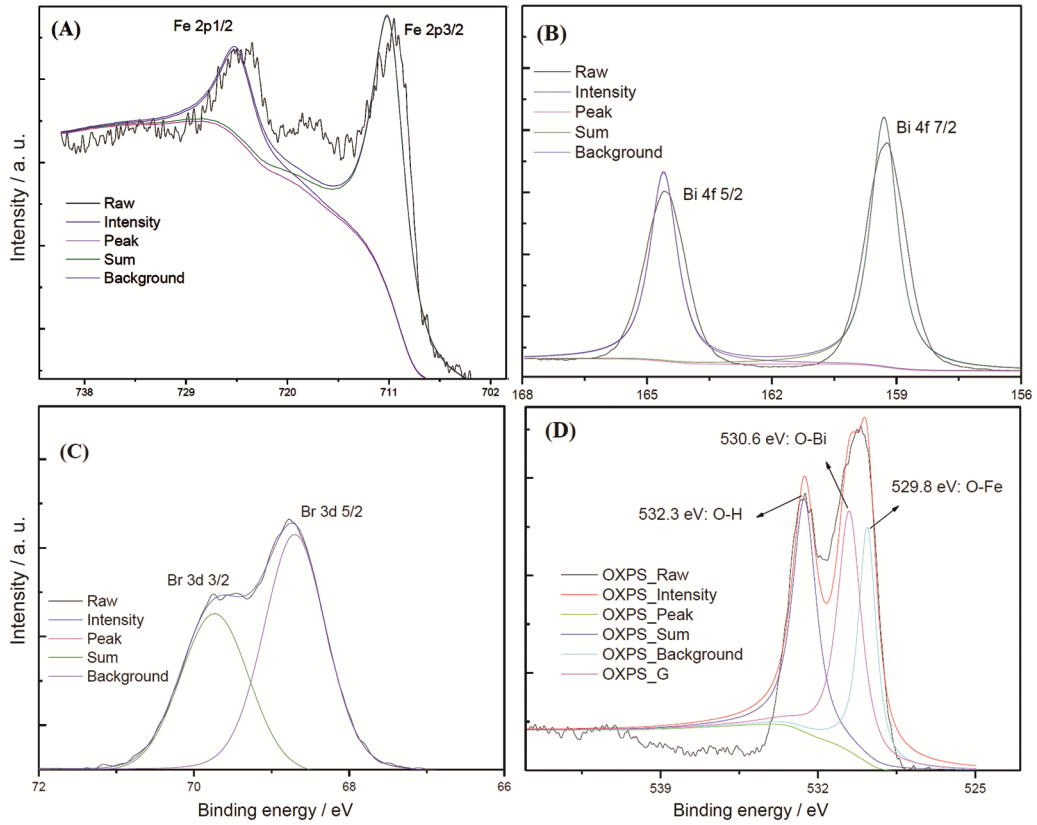

Fig. 4 — The high-resolution core level XPS spectra of BiOBr@Fe_3O_4 sample, from which (A) Fe 2p, (B) Bi 4f, (C) Br 3d and (D) O 1s.

satellite peak on Fe 2p3/2 could be found for Fe_3O_4, which confirming the Fe^{2+} and Fe^{3+} were included in Fe_3O_4. The peaks appear at 164.6 eV and 159.3 eV was assigned to Bi 4f5/2 and Bi 4f7/2 (Fig. 4B), respectively, which was attributed to the characteristic of Bi^{3+} in BiOBr. High-resolution XPS spectrum of Br 3d (Fig. 4C) show that the peaks located at binding energies of 69.7 and 68.7 eV, which correspond to Br element of 3d3/2 and Br 3d5/2 state of BiOBr, respectively. For oxygen element, the XPS profile in Fig. 4D can be divided into the following three peaks. The peaks of O 1s at 532.3 eV can be assigned to the hydroxyl anion or hydroxyl group (—OH) on the surface adsorption of water molecule. The peaks of O 1s at 529.8 eV and 530.6 eV were ascribed to O—Fe and O—Bi bonds, respectively. The above measurements reveal the BiOBr@Fe_3O_4 hybrid consists of BiOBr and Fe_3O_4, which accords with the previous XRD and FTIR results.

Optical, electrical and magnetic properties

Figure 5 is an ultraviolet-visible DRS spectra of Fe_3O_4, BiOBr and BiOBr@Fe_3O_4samples. It can be seen from the graph that Fe_3O_4 has very excellent light absorption capability in the visible light region, and BiOBr has slightly weaker absorption capability in the visible light. Nonetheless, after the combination of the two components of Fe_3O_4 and BiOBr, BiOBr@Fe_3O_4 composite show light absorption capability between the above two semiconductors. It can be drawn that after Fe_3O_4 is coupled with BiOBr, the visible light absorption capability of pure BiOBr is significantly improved.

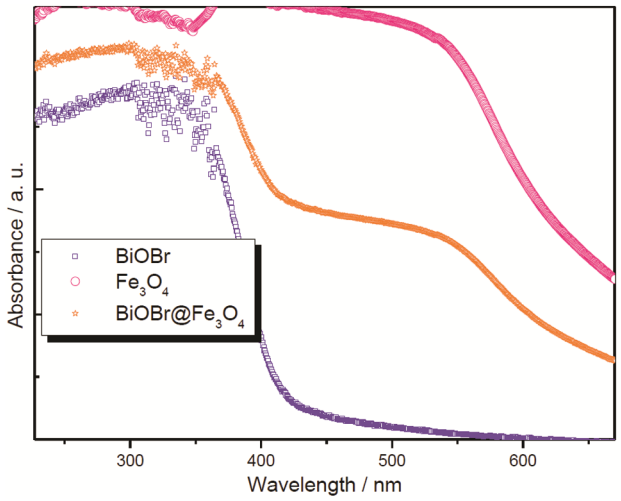

Fig. 5 — UV-vis diffuse reflection spectra of Fe_3O_4, BiOBr and BiOBr@Fe_3O_4 samples.

Figure 6 is as-obtained steady-state fluorescence emission spectra of Fe_3O_4, BiOBr and BiOBr@Fe_3O_4 that excited under 330nm ultraviolet light. Generally, lower the fluorescence emission intensity, lower is the electron-hole recombination probability of the catalyst. From the picture, it can be seen that the fluorescence intensity of Fe_3O_4 is the highest, while BiOBr is slightly lower, and the fluorescence intensity of BiOBr@Fe_3O_4 is the lowest, indicating that the combination of the two reagents effectively reduces the coincidence rate of photogenerated electrons and holes, so the photocatalytic efficiency of the BiOBr@Fe_3O_4 catalyst is expected to be higher than that of BiOBr alone. Figure 7 provided the room-temperature magnetic hysteresis loops of the

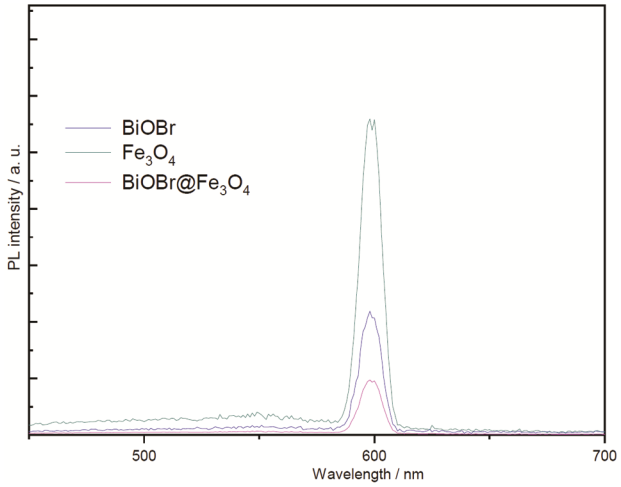

Fig. 6 — Steady-state PL spectra of as-prepared materials (A) and the time-resolved PL spectra (B) of BiOBr and BiOBr@Fe_3O_4 samples.

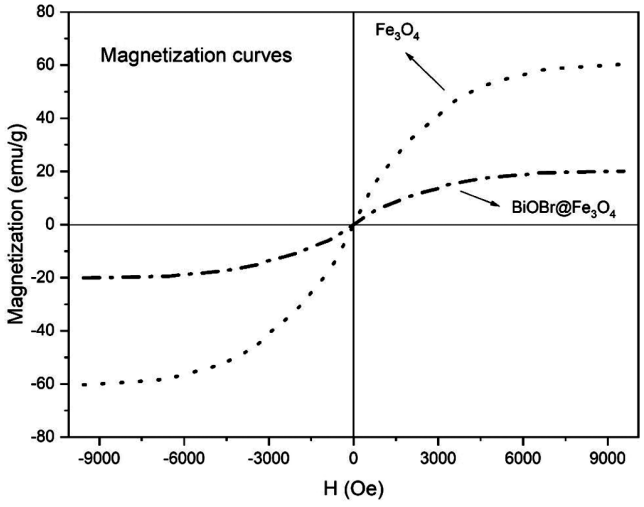

Fig. 7 — The room-temperature magnetic hysteresis loops for the as-made Fe_3O_4 NPs, and the BiOBr@Fe_3O_4 hybrid materials.

as-made materials, and these materials exhibited typical ferro-magnetic behaviour. The saturation magnetization saturation (Ms) values for the Fe_3O_4 NPs and BiOBr@Fe_3O_4 nanocomposites are 60.7 and 20.0 emu/g, respectively. It was noteworthy that the Msvalue of BiOBr@Fe_3O_4 nanocomposites were much lower than that of the Fe_3O_4 NPs, which was ascribed to the existence of nonmagnetic BiOBr in the total mass. Given the small remanence and coercivity, the Fe_3O_4 NPs and BiOBr@Fe_3O_4 nanocomposites exhibited supe rpara magnetic behaviour. Strong magnetization of the hetero structured BiOBr@Fe_3O_4 photocatalyst allowed it to be rapidly and conveniently separated from an aqueous solution by applying an external magnetic field.

Photocatalytic reaction and physical mechanism

Photocatalytic activity of samples was evaluated by photodegradation of MB under visible light (λ≥420 nm). Firstly, the absorbance of the samples collected during the degradation of MB solution was measured with an ultraviolet-visible spectrophotometer. The measurement results are plotted in the following graph (Fig. 8a), in which the absorbance of Fe_3O_4, BiOBr and BiOBr@Fe_3O_4 for catalyze degradation of MB solution are given respectively. As can be seen, with the extension of the reaction time, the absorbance of the MB solution is gradually decreasing. It is obvious that the single-phase Fe_3O_4 exhibited a poor catalytic activity, which might be ascribed to a high carrier recombination rate caused by the defect-state energy levels. However, it is still found that Fe_3O_4 has certain photodegradation ability to MB, which is attributed to the fact that Fe_3O_4 can absorb visible light, and is also likely to have a great relationship with its ability to generate active radicals. It can be obtained that Fe_3O_4 has certain photodegradation ability to MB. It is clear that the absorbance of Fe_3O_4 and BiOBr for the catalytic degradation of MB solution gradually decreases, but the difference between the three is not very large. Conversely, the absorbance of BiOBr@Fe_3O_4 hybrid for the degradation of MB is much larger than that of BiOBr or Fe_3O_4 alone. This shows that the degradation efficiency of BiOBr@Fe_3O_4hybrid photocatalyst is the highest, and it can be seen on the way that MB is basically completely degraded by BiOBr@Fe_3O_4 hybrid within 60 min, which also shows that the catalytic effect of BiOBr@Fe_3O_4 composite is excellent. There is also a catalytic effect diagram in this diagram. This is the solution obtained by BiOBr@Fe_3O_4 hybrid in catalyzing MB at different times. With the passage of time, the colour gradually becomes lighter. The effect becomes more and more obvious after 60 min, which can also show the good catalytic effect. There is also a catalytic effect picture in this picture. This is the solution taken by BiOBr@Fe_3O_4 composite to catalyze MB solution at different times. With the passage of time, the colour becomes obviously lighter, and the catalytic effect is good.

In order to investigate the stability of BiOBr@Fe_3O_4 photocatalyst, the photodegradation stability test is carried out by centrifuge to recover the photocatalyst and fully drying the photocatalyst, and then carrying out the next cycle degradation, wherein the degradation conditions are the same as before, and the cycle times are 5 times. In detail, the sample was

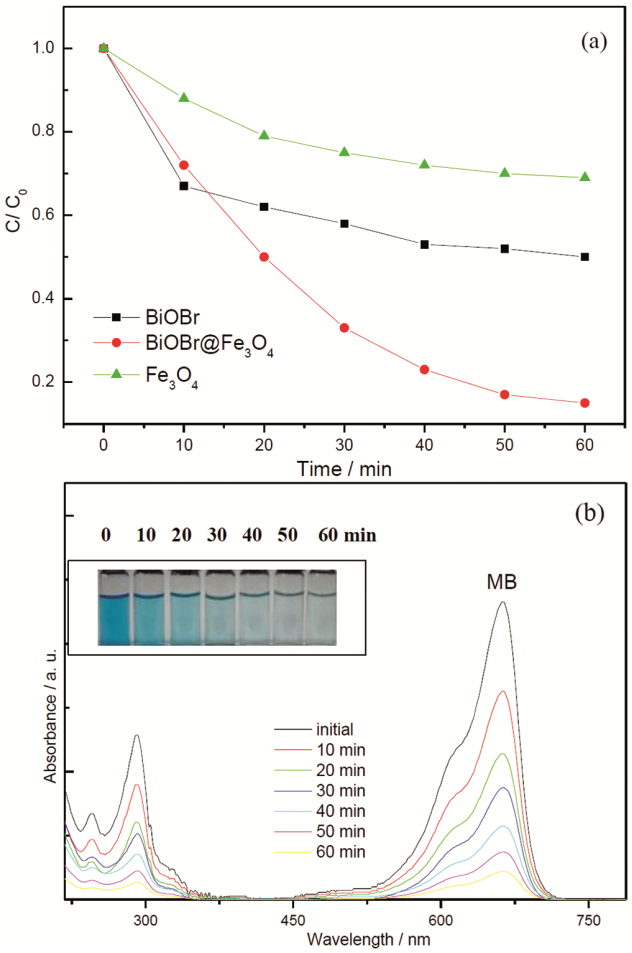

Fig. 8 — Comparison of photocatalytic activities of different samples for MB degradation (a) within 60 minutes using visible light (λ>420 nm), and (b) absorption changes of MB solution in the presence of BiOBr@Fe_3O_4 hybrid material.

circulated for 5 times under the same experimental conditions. After each cycle, the sample was washed with ethanol and deionized water and dried at 80°C for later use. As expected, the employed BiOBr@Fe_3O_4 hybrid material could be easily separated from an aqueous solution using permanent magnet by virtue of their excellent magnetic properties. Then the regenerated photocatalyst was thoroughly washed and dried at 80°C for a recycle purpose according to the designed procedure. It can be observed from Fig. 9 that the photocatalytic performance of all the BiOBr@Fe_3O_4 hybrid in terms of MB removal well maintains and only exhibits trivial decreases in performances after five cycles, which imply that the BiOBr@Fe_3O_4 composite is quite stable for reproducibility. Overall, the degradation rate of MB was ~80% for the fifth time, and the results showed that the composite catalyst had excellent stability. After 5 times of recycling, the degradation rate of photocatalytic MB can still be kept above 80%, indicating that the composite catalyst has good photocatalytic stability and reusability.

In order to analysis the mechanism of the photocatalytic reaction, reactive species trapping experiments were performed. Four groups of experiments were conducted, whereas 3 mL isopropyl alcohol (ISA), Na_2SO_3, $K_2Cr_2O_7$ and formic acid were added into photocatalytic system respectively, which were used as sacrificial agents to consume the *OH, photoinduced holes, e– and $*O_2^-$. The photocatalytic degradation experiment of MB aqueous solution was carried out according to the above steps. The effect of various involved capture agents on the photodegradation rate of MB is given in Fig. 10. The results showed that the introduction of $K_2Cr_2O_7$ scavenger had no obvious inhibition on the degradation process of the reaction system. Similarly, the photocatalytic activity of BiOBr@Fe_3O_4system did not change obviously after Na_2SO_3 was added. It tells that holes (h^+) and photogenerated electrons (e^-) are not the main active species in photocatalytic process since the photodegradation ability was not significantly affected. However, the photocatalytic activity was reduced and the photocatalytic effect was greatly inhibited after adding formic acid and ISA in the experiment of photocatalytic degradation of MB. When ISA is added, the photocatalytic degradation ratio of MB is obviously reduced. The photocatalytic degradation ratio of MB is 32% after 60 min of illumination. Meanwhile, when formic acid is added, the photocatalytic degradation rate of MB is also reduced. The photocatalytic degradation ratio of MB is slightly reduced to 69% after 60 min of illumination, which proving that the number of active groups in it was reduced and captured. The results showed that the introduction of ISA led to a significant reduction in the photocatalytic degradation effect of the system after 60min of reaction compared with the sample without quencher, and the reduction was the most significant with the final degradation ratio less than 35%. Summarize the above experimental facts, it can be speculated that h^+ or e^-including $*O_2^-$ was not

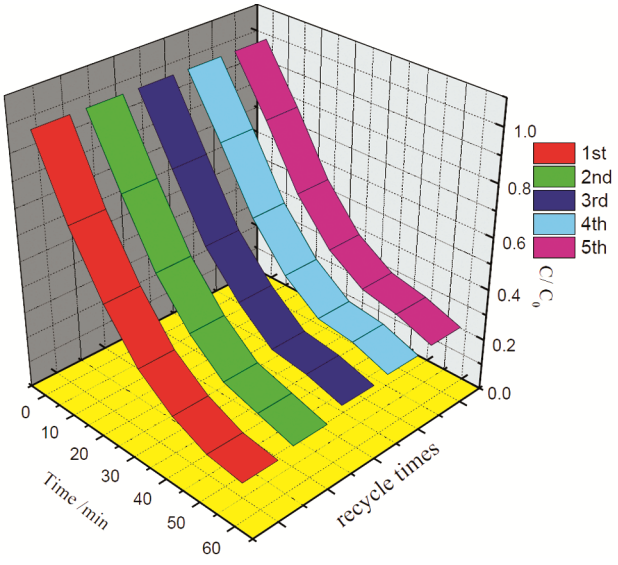

Fig. 9 — Recycle experiments of BiOBr@Fe_3O_4 hybrid material for degradation of MB under visible light illumination.

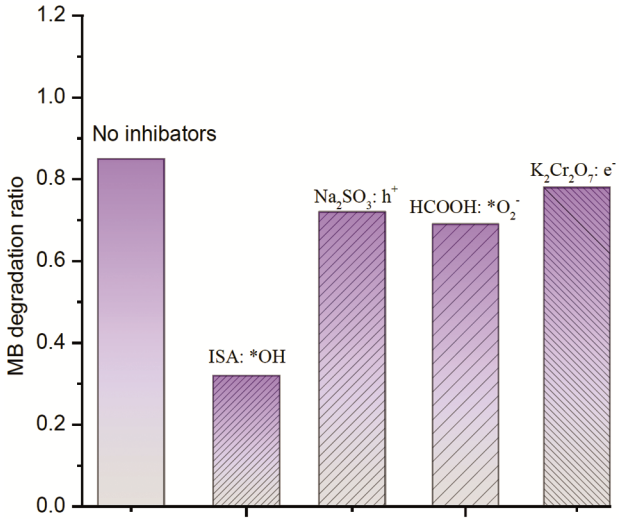

Fig. 10 — The effects of a series of inhibitors on the photocatalytic efficiency of BiOBr@Fe_3O_4 hybrid material for MB removal.

the main active species of photocatalytic reaction, whereas *OH was the main active species and these active species play a certain role in photocatalytic degradation system. Moreover, the photocatalytic activity almost disappeared after the capture agent ISA was added, indicating that most of the photocatalytic system was captured by the capture agent and resulting in a decrease in the catalytic activity of the photocatalytic material. Therefore, *OH occupies a dominant position and acts a pivotal role in the current photocatalytic reaction system, and at the same time, there are some active groups such as $*O_2^-$, which are the basis for photocatalytic degradation of MB, and the possible mechanism of photocatalytic reaction can be inferred as below.

In this work, the improved photocatalytic efficiency was indeed depends on efficient generation, separation and transfer of the photo-induced h^+/e^- pairs, which mainly depends on the band structure of the hybrid material. It is known Fe_3O_4 belongs to n-type semiconductor, whereas BiOBr belongs to a p-type semiconductor. Thus, a positive charge carriers (h^+/e^-) separation could be achieved and this will minimize the recombination chance of photoexcited h^+/e^- pairs due to the formation of p-n junction at the interface of the different components. It was reported that the conduction band (CB) and valence band (VB) potential of Fe_3O_4 are 0.16 eV and 0.28 eV (vs. NHE), respectively. Moreover, the conduction band (CB) and valence band (VB) potential of BiOBr are 0.35 eV and 2.93 eV (vs. NHE), respectively. Energy band structures of Fe_3O_4 match rightly with that of BiOBr, which is favour to the separation and transfer of h^+/e^- pairs at the interface of the heterojunction. Once the electrons in the VB of BiOBr and Fe_3O_4 are excited to the CB under visible light source, the photo-induced electrons on the CB of Fe_3O_4 would transfer to the CB of BiOBr while the photo generated holes on the VB of BiOBr would transfer to the VB of Fe_3O_4 via traditional mechanism. These resulted in massive of electrons stay on the CB of BiOBr surface and holes on the VB of Fe_3O_4. Through this way, the photogenerated carriers could be separated efficiently and improve the photocatalytic activities of BiOBr/Fe_3O_4. Nonetheless, electrons in CB of BiOBr (E_{CB}= 0.35 eV) cannot react with O_2 adsorbed on the surface of catalyst to generate reactive $*O_2^-$ since $E(O_2/*O_2^-)$= -0.046 eV (vs. NHE), which is negative for electrons in CB of BiOBr to reduce them via two-electron reduction process. Besides, O_2 gets electrons, is difficult in the degradation of organic matter because of its poor capability. Meanwhile, h^+ in the VB of Fe_3O_4 (E_{VB}= +0.28 eV) is also not positive enough to react with OH− and finally generate reactive •OH since E(OH− /•OH)= +2.38 eV (vs. NHE).On the basis of previous analysis, a possible Z-scheme charge carrier transfer mechanism in photocatalysis was proposed. Namely, the photoinduced electrons in the conduction band (CB) of BiOBr could transfer to the VB of Fe_3O_4 via built-in electric field formed between the interfaces of BiOBr@Fe_3O_4 heterojunction. Then these e— will combine with the photoexcited h+ at the VB of Fe_3O_4 according to a Z-scheme transfer mechanism. At last, repeated attacks MB dye molecules by the •OH that formed at the VB of BiOBr will be possible since the potential of BiOBr valence band (+2.93 eV vs. NHE) is more positive than the potential of OH− /•OH (+2.38 eV vs. NHE). Therefore, it leads to a successful removal of MB, and •OH radicals become main species in the photocatalytic reaction and play a crucial role, which is in line with the previous experimental results.

Conclusion

In brief, a magnetically recyclable BiOBr@Fe_3O_4 hybrid material has been successfully prepared by a simple chemical method. Aqueous MB was selected to check the photocatalytic performance of as-synthesized catalysts. According to the photocatalytic results, the BiOBr@Fe_3O_4 composite displayed significantly enhanced efficiency in eliminate MB than the single-phase Fe_3O_4 NPs or pure BiOBr. It is speculated that the synergistic effect between the two oxides comes from electron transfer between BiOBr and Fe_3O_4. Synergy via Z-type of charge carrier transfer mechanism will be applied in many fields, such as photolysis of water and photochemical batteries, water overall splitting and large scale environmental purification.

Acknowledgements

This work was supported by Natural Science Foundation of Hubei Province of China (Project No. 2011CDB148).

References

1 Hu Y, Peng X, Ai Z H, Jia F L & Zhang L Z, *Environ Sci Technol*, 53 (2019) 8333.

2 Zhang G K, Gao Y Y, Zhang Y L & Guo Y D, *Environ Sci Technol*, 44 (2010) 6384.

3 Wang X B, Chen N & Zhang L Z, *Environ Sci Nano*, 6 (2019) 2185.
4 Li H, Shang H, Li Y H, Cao X M, Yang Z P, Ai Z H & Zhang L Z, *Environ Sci Technol*, 53 (2019) 6964.
5 Mao C L, Wang J X, Zou Y J, Li H, Zhan G M, Li J, Zhao J C & Zhang L Z, *Green Chem*, 21 (2019) 2852.
6 Shang H, Li M Q, Li H, Huang S, Mao C L, Ai Z H & Zhang L Z, *Environ Sci Technol*, 53 (2019) 6444.
7 Sun H W, Wang J, Jiang Y, Shen W J, Jia F L, Wang S H, Liao X M & Zhang L Z, *Environ Sci Technol*, 53 (2019) 3707.
8 Mu Y, Zhan G M, Huang C M, Wang X B, Ai Z H, Zou J P, Luo S L & Zhang L Z, *Environ Sci Technol*, 53 (2019) 3208.
9 Huang X P, Hou X J, Wang F, Guo B H, Song F H, Ling L, Zhao J C & Zhang L Z, *Environ Sci Nano*, 6 (2019) 892.
10 Zhang L Z & Yu J C, *Catal Commun*, 6 (2005) 684.
11 Wang Y B, Zhang Y N, Zhao G H, Wu M F, Li M F, Li D M, Zhang Y G & Zhang Y L, *Sep Purif Technol*, 104 (2013) 229.
12 Zhang Y L, Deng L J, Zhang G K & Gan H H, *Colloids Surf A*, 384 (2011) 137.
13 Zhang Y L, Wang D J & Zhang G K, *Chem Eng J*, 173 (2011) 1.
14 Wang Y J, Zhao H Y, Gao J X, Zhao G H, Zhang Y G & Zhang Y L, *J Phys Chem C*, 116 (2012) 7457.
15 Li D Y, Zhang Y G, Zhang Y L, Zhou X F & Guo S J, *J Hazard Mater*, 258 (2013) 42.
16 Zhang X, Ai Z H, Jia F L, Zhang L Z, Fan X X & Zou Z G, *Mater Chem Phys*, 103 (2007) 162.
17 Zhang Y L, Li D Y, Zhang Y G, Zhou X F, Guo S J & Yang L B, *J Mater Chem A*, 2 (2014) 8273.
18 Wan Z, Zhang G K, Wang J T & Zhang Y L, *RSC Adv*, 3 (2013) 19617.
19 Guo Y D, Zhang G K, Liu J & Zhang Y L, *RSC Adv*, 3 (2013) 2963.
20 Wen Z P, Zhang Y L, Dai C M & Sun Z, *J Hazard Mater*, 287 (2015) 225.
21 Zhang L Z, Djerdj I, Cao M H, Antonietti M & Niederberger M, *Adv Mater*, 19 (2007) 2083.
22 Zhang Y L, Guo Y D, Zhang G K & Gao Y Y, *Appl Clay Sci*, 51 (2011) 335.
23 Xu H, Zheng Z, Zhang L Z, Zhang H L & Deng F, *J Solid State Chem*, 181 (2008) 2516.
24 Abdelhafeez Islam A, Yao Q F, Wang C X, Su Y M, Zhou X F & Zhang Y L, *Sustainable Energy Fuels*, 3 (2019) 1764.
25 Liu Z G, Sun P Z, Pavlostathis Spyros G, Zhou X F & Zhang Y L, *Bioresour Technol*, 150 (2013) 28.
26 Shen Z, Gu M Y, Zhang M, Sang W J, Zhou X F, Zhang Y L & Jin F M, *RSC Adv*, 4 (2014) 15256
27 Shen Z, Kong L, Zhang W, Gu M Y, Xia M, Zhou X F & Zhang Y L, *RSC Adv*, 9, (2019) 18989.
28 Zhang Y L, Shen Z, Zhou X F, Zhang M & Jin F M, *Green Chem*, 14 (2012) 3285.
29 Zhang Y, Fu M, Wu D L & Zhang Y L, *RSC Adv*, 7 (2017) 13398.
30 Shen Z, Zhang Y L & Jin F M, *Green Chem*, 13 (2011) 820.
31 Wen Z P, Dai C M, Zhu Y & Zhang Y L, *RSC Adv*, 5 (2015) 4058.
32 Shen Z, Zhang Y L & Jin F M, *RSC Adv*, 2 (2012) 797.
33 Xia M, Dong W J, Gu M Y, Chang C, Shen Z & Zhang Y L, *RSC Adv*, 8 (2018) 8965.
34 Zhang Y L, Gan H H & Zhang G K, *Chem Eng* J, 172 (2011) 936.
35 Guo Y D, Zhang G K, Gan H H & Zhang Y L, *Dalton Trans*, 41 (2012) 12697.
36 Guo S J, Li D Y, Zhang Y L, Zhang Y G & Zhou X F, *Electrochim Acta*, 121 (2014) 352.
37 Qiao H, Wang Y W, Xiao L F & Zhang L Z, *Electrochem Commun* 10 (2008) 1280.
38 Hu Y, Zheng Z, Jia H M, Tang Y W & Zhang L Z, *J Phys Chem C*, 112 (2008) 13037.
39 Xiao H Y, Li P N, Jia F L & Zhang L Z, *J Phys Chem C*, 113 (2009) 21034.
40 Xiao L F, Zhao Y Q, Yin J & Zhang L Z, *Chem Eur J*, 15 (2009) 9442.
41 Xiao H Y, Ai Z H & Zhang L Z, *J Phys Chem C*, 113 (2009) 16625.
42 Wang Y W, Huang Y, Ho W K, Zhang L Z, Zou Z G & Lee S C, *J Hazard Mater*, 169 (2009) 77.
43 Huang Y, Ho W K, Ai Z H, Song X, Zhang L Z & Lee S C, *Appl Catal B*, 89 (2009) 398.
44 Wang Y W, Zhang L Z, Li S & Jena P, *J Phys Chem C*, 113 (2009) 9210.
45 Jia H M, Zheng Z, Zhao H X, Zhang L Z & Zou Z G, *Mater Res Bull*, 44 (2009) 1312.
46 Zhang X, Zhang L Z, Xie T F & Wang D J, *J Phys Chem C*, 113 (2009) 7371.
47 Zhao K, Zhang X & Zhang L Z, *Electrochem Commun*, 11 (2009) 612.
48 Xu H & Zhang L Z, *J Phys Chem C*, 113 (2009) 1785.
49 Wang K W, Jia F L, Zheng Z & Zhang L Z, *Electrochem Commun*, 12 (2010) 1764.
50 Gong J M, Wang L Y, Miao X J & Zhang L Z, *Electrochem Commun*, 12 (2010) 1658.
51 Yang L G, Wang L Z, Xing M Y, Lei J Y & Zhang J L, *Appl Catal B*, 180 (2016) 106.
52 Lin A N, Qi D Y, Ding H, Wang L Z, Xing M Y, Shen B & Zhang J L, *Catal Today*, 281 (2017) 636.
53 Liu F H, Yu J, Tu G Y, Qu L, Xiao J C, Liu Y D, Wang L Z, Lei J Y & Zhang J L, *Appl Catal* B, 201 (2017) 1.
54 Du D, Shi W, Wang L Z & Zhang J L, *Appl Catal B*, 200 (2017) 484.
55 Xing M Y, Xu W J, Dong C C, Bai Y C, Zeng J B, Zhou Y, Zhang J L & Yin Y D, *Chem*, 4 (2018) 1359.
56 Qiu B C, Deng Y X, Li Q Y, Shen B, Xing M Y & Zhang J L, *J Phys Chem C,* 120 (2016) 12125.
57 Fang W Z, Dappozze F, Guillard C, Zhou Y, Xing M Y, Mishra S, Daniele S & Zhang J L, *J Phys Chem C*, 121 (2017) 17068.
58 Dong C Y, Xing M Y & Zhang J L, *J Phys Chem Lett*, 7 (2016) 2962.
59 Yang L G, Cui C F, Wang L Z, Lei J Y & Zhang J L, *ACS Appl Mater Interfaces*, 8 (2016) 19084.
60 Shi W, Du D, Shen B, Cui C F, Lu L J, Wang L Z & Zhang J L, *ACS Appl Mater Interfaces*, 8 (2016) 20831.
61 Zhou Y, Yi Q Y, Xing M Y, Shang L, Zhang T R & Zhang J L, *Chem Commun*, 52 (2016) 1689.

62 Nasir M, Lei J Y, Iqbal W & Zhang J L, *Appl Surf Sci*, 364 (2016) 446.
63 Tan X J, Wang L Z, Cheng C, Yan X F, Shen B & Zhang J L, *Chem Commun*, 52 (2016) 2893.
64 Wu Q F, Bao S Y, Tian B Z, Xiao Y F & Zhang J L, *Chem Commun*, 52 (2016) 7478.
65 Dong C Y, Xing M Y & Zhang J L, *Mater Horiz*, 3 (2016) 608.
66 Bao S Y, Wang Z Q, Gong X Q, Zeng C Y, Wu Q F, Tian B Z & Zhang J L, *J Mater Chem* A, 4 (2016) 18570.
67 Wang L Z, Xu Y, Tan X J, Tapas S & Zhang J L, *RSC Adv*, 7 (2017) 36201.
68 Zhang P, Liu Y, Tian B Z, Luo Y S & Zhang J L, *Catal Today*, 281 (2017) 181.
69 Peng Y L, Wang L Z, Liu Y D, Chen H J, Lei J Y & Zhang J L, *Eur J Inorg Chem*, 40 (2017) 4797.
70 Zhang J L, Wu Y M, Xing M Y, Leghari S A K & Sajjad S, *Energy Environ Sci*, 3 (2010) 715.
71 Li Q Y, Li T Y, Chang S Z, Tao Q S, Tian B Z & Zhang J L, *Cryst Eng Comm*, 18 (2016) 5074.
72 Dong C C, Song H, Zhou Y, Dong C Y, Shen B, Yang H, Matsuoka M, Xing M Y & Zhang J L, *RSC Adv*, 6 (2016) 77863.
73 Fang W Z, Zhou Y, Dong C C, Xing M Y & Zhang J L, *Catal Today*, 266 (2016) 188.
74 Zhang G K, Shen X & Yang Y Q, *J Phys Chem C*, 115 (2011) 7145.
75 Wang J, Wang J T, Wu X Y & Zhang G K, *Mater Res Bull*, 96 (2017) 262.
76 Zhang G K, Ding X M, Hu Y J, Huang B B, Zhang X Y, Qin X Y, Zhou J & Xie J W, *J Phys Chem C*, 112 (2008) 17994.
77 Fang W Z, Xing M Y & Zhang J L, *J Photochem Photobiol C*, 32 (2017) 21.
78 Yuan X L, Zhang J L, Tian B Z, Anpo M & He D N, *Res Chem Intermed*, 35 (2009) 693.
79 Hao H Y & Zhang J L, *Mater Lett*, 63 (2009) 106.
80 Xu H & Zhang L Z, *J Phys Chem C*, 114 (2010) 11534.
81 Xu H & Zhang L Z, *J Phys Chem C*, 114 (2010) 940.
82 Xing M Y, Zhang J L & Chen F, *Appl Catal B*, 89 (2009) 563.
83 Wu X Y, Li K Q, Li Y & Zhang G K, *Nanoscale*, 10 (2018) 15294.
84 Tian B Z, Li C Z, Gu F, Jiang H B, Hu Y J & Zhang J L, *Chem Eng J*, 151 (2009) 220.
85 Ji P F, Zhang J L, Chen F & Anpo M, *Appl Catal B*, 85 (2009) 148.
86 Li Y, Wu X Y, Li J, Wang K & Zhang G K, *Appl Catal B*, 229 (2018) 218.
87 Li J, Zhang L Z, Li Y J & Yu Y, *Nanoscale*, 6 (2014) 167.
88 Zhang X, Zhang L Z, Xie T F & Wang D J, *J Phys Chem C*, 113 (2009) 7371.
89 Wang Y N, Deng K J & Zhang L Z, *J Phys Chem C*, 115 (2011) 14300.
90 Jiang J & Zhang L Z, *Chem Eur J*, 17 (2011) 3710.
91 Li H, Qin F, Yang Z P, Cui X M, Wang J F & Zhang L Z, *J Am Chem Soc*, 139 (2017) 3513.
92 Li H, Shang J, Ai Z H & Zhang L Z, *J Am Chem Soc*, 137 (2015) 6393.
93 Ge S X & Zhang L Z, *Environ Sci Technol*, 45 (2011) 3027.
94 Jiang J, Zhao K, Xiao X Y & Zhang L Z, *J Am Chem Soc*, 134 (2012) 4473.
95 Zhao K, Zhang L Z, Wang J J, Li Q X, He W W & Yin J J, *J Am Chem Soc*, 135 (2013) 15750.
96 Jiang J, Zhang L Z, Li H, He W W & Yin J J, *Nanoscale*, 5 (2013) 10573.
97 Xiao X Y, Jiang J & Zhang L Z, *Appl Catal B*, 142 (2013) 487.
98 Wang J L, Yu Y & Zhang L Z, *Appl Catal B*, 136 (2013) 112.
99 Jiang J, Zhang X, Sun P B & Zhang L Z, *J Phys Chem C*, 115 (2011) 20555.
100 Zhang X & Zhang L Z, *J Phys Chem C*, 114 (2010) 18198.
101 Li H, Shi J G, Zhao K & Zhang L Z, *Nanoscale*, 6 (2014) 14168.
102 Li H & Zhang L Z, *Nanoscale*, 6 (2014) 7805.